Feasibility of utilizing three-dimensional nanoarchitecture to endow metal sulfides with superior Li+ storage capability

CrossMark

Xiaomeng Wu, Shichao Zhang*, Hua Fang, Zhijia Du, Ruoxu Lin

School of Materials Science and Engineering, Beijing University of Aeronautics and Astronautics, Beijing 100191, China

H I G H L I G H T S

- Arrayed SnS@Cu core–shell nanowires were engineered for Li+ storage application.
- The reversible capacity is 347 mAh g^{-1} (3.3C) even after 80 rate-varying cycles.
- Innovative electrochemical fabrication of SnS/CuS nanotubes array was achieved.
- Designed 3D architecture can boost application of metal sulfides in smart energy storage.

A R T I C L E   I N F O

A B S T R A C T

Three-dimensional (3D) nanoarchitectures have demonstrated substantial advantages in capturing the performance of traditional electrode materials. In this regard, novel Cu@SnS core–shell nanowire array is fabricated via a rational electrochemical assembly strategy. Meanwhile it is also discovered that striking structural and compositional evolution from Cu@SnS core–shell nanowires to hybrid CuS/SnS nanotubes can be achieved by a simple tuning of reaction conditions. As a proof of concept, long-term cycling stability and remarkable rate capability are exhibited by Cu@SnS nanoelectrode in the study of its Li+ storage properties (e.g., it delivers a capacity of ∼347 mAh g^{-1} at 3.33C even after 80 rate-varying cycles), which verifies the effectiveness of the designed 3D configuration in tackling possible electrical/mechanical failures of the electrode during repeated Li+ uptake/release process. Moreover, because of their potential for achieving high power and energy densities on a small footprint area, the designed metal sulfide nanoelectrodes may be promisingly applied in microenergy storage devices.

1. Introduction

The development of future-generation Li-ion microbatteries with high capacity and excellent rate capability is of great technological importance for downscaling a variety of electronic microsystems, such as microsensors, medical implants, self-powered integrated circuits or microelectromechanical systems (MEMS) [1–3]. In addition to searching for compositionally new electrode materials, rational design and construction of electrode materials with 3D nanoarchitectured configurations have also gained considerable attention for advanced Li-ion batteries, since they could offer unprecedented opportunities for tackling the essential problems related to mass and charge transport kinetics as well as electrode stability [4,5].

Among the variety of metal sulfides, tin monosulfide (SnS) is of particular interest for fabricating devices in both fields of energy conversion and storage because of its competitive chemical and physical properties [6,7]. In particular, SnS has a higher theoretical lithium-storage capacity (782 mAh g^{-1}) compared with its intensively investigated "sister-material" SnS$_2$ [8,9], but until recently limited progress has been made towards optimizing the design of SnS-based nanoelectrodes, especially those grown directly on conducting substrates, for Li-ion battery application [10–14]. Thus far, studies have shown that electrodeposition is a feasible and convenient way for preparing SnS films [15–17], nevertheless, apart from electrochemical synthesized SnS thick films have poor interfacial adhesion and thus is very easy to peel off the planar metal substrate, the finite and non-uniform distribution of potential or current across the semiconducting deposits remains a substantial obstacle for the uniform deposition of SnS dense films with a certain thickness, thereby greatly limiting their electrochemical performance and applicability [18]. Moreover, despite benefits

* Corresponding author. Tel.: +86 10 82338148; fax: +86 10 82339319.
  E-mail address: csc@buaa.edu.cn (S. Zhang).
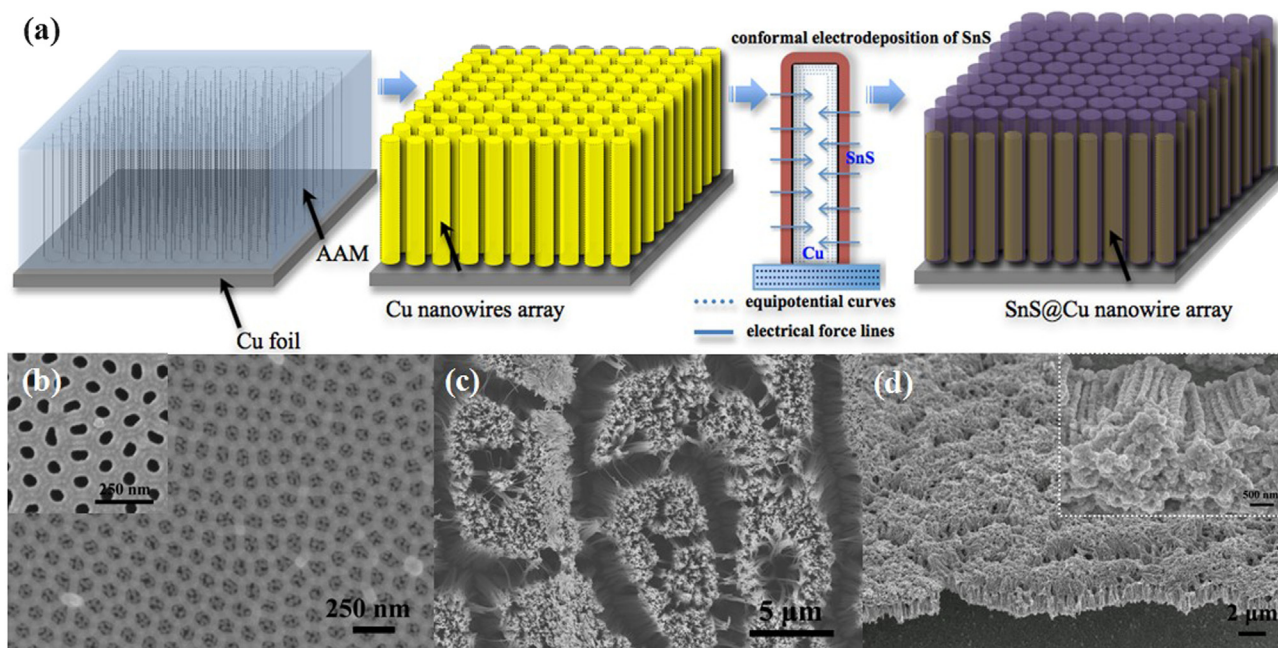
Fig. 1. (a) Schematic describing the fabrication process of the 3D-patterned Cu@SnS nanoelectrode. (b) FESEM image of AAM template (inset is bottom view), (c) Cu nanowires array, (d) overview of the Cu@SnS nanowire forest with a magnified cross-sectional image shown inset.

derived from rationally design nanostructured materials with shortened diffusion length and large surface area, it is still challenging to effectively reduce the high probability of nanostructured film-type SnS electrodes suffering from electrical/mechanical failures during Li$^+$ uptake/release as making them thicker to store more energy, and the issue represents a key consideration for constructing future-generation Li-ion microbatteries [1]. Therefore, it is very meaningful to find a general solution for the above-mentioned problems.

Taking inspiration from the pioneering work of Tarascon et al. towards creating 3D nanoarchitectured electrode for high-performance Li-ion batteries [19–21], herein, we aimed at utilizing aligned Cu nanowires with large electroactive area to boost the electrochemical synthesis of high-quality SnS on limited footprint area. Essentially, this design means large amount of electrochemical energy can be stored within limited footprint areas, and the resulting Cu@SnS nanoelectrode is capable of being charged/discharged efficiently at high current rates when used as an anode material in Li-ion battery. Meanwhile, we also discovered that novel CuS/SnS nanotube array could be electrochemically synthesized by using copper nanowires as self-sacrificial templates. Owing to its unique hollow structure and tunable composition, such metal sulfide nanotube array may also hold promise for use as nanoelectrode in Li-ion microbatteries. Moreover, we hope that such findings will shed light on the synthesis of other copper related bimetal sulfides with well-aligned tubular nanostructures for energy-related applications.

2. Experimental section

Highly regular through-hole anodic alumina membranes (AAMs) with different pore diameters ranged from 50 nm to 80 nm were fabricated by method previously reported [22]. Then, the polished cathode Cu foil, AAM, cellulose paper separator, and the anode Cu foil were tightly packed in sequence and assembled using two stainless steel clamps, and then electrodeposition of Cu

nanowire array was achieved using a current pulsing approach with a cathodic pulse (−50 mA, 25 ms), and a relaxation time (0 mA, 250 ms) in a conventional acid copper sulfate based solutions (CuSO$_4$.5H$_2$O 200 g l^{-1}, H$_2$SO$_4$ 90 g l^{-1}) in room temperature. Afterward, aligned Cu nanowires was released from AAM by dissolving the template in 1 M NaOH solution for the sequential deposition or synthetic process. (i) *Fabrication of Cu@SnS nanowire arrays.* We adopted a potential pulsing approach for the conformal coating of SnS onto Cu nanowires array, which was archived with a cathodic pulse (−1.0 V, 10 s) followed by an anodic pulse (+0.1 V, 10 s) in a deaerated electrolyte bath contained 5 mM SnCl$_2$, 25 mM Na$_2$S$_2$O$_3$ (SnCl$_2$ was dissolved in 3 ml of acetone prior to mixing with aqueous solution and pH of the solution was adjusted to ∼3.0 by adding HCl) after vacuum-assisted impregnation. The total deposition period was 10–20 min, then the deposits were washed softly and dried at 100 °C for 2 h in vacuum. (ii) *Fabrication of CuS/ SnS nanotube arrays.* The synthetic procedure and electrolyte system were similar to those of SnS deposition, except that the reaction temperature was elevated to 65 °C together with the as-prepared sample was heat treated at 150 °C for 1 h under inert atmosphere.

The resulting samples were characterized by X-ray diffraction (XRD), Raman spectra, field emission scanning electron microscopy (FESEM), transmission electron microscopy (TEM), energy dispersive X-ray spectroscopy (EDX) and X-ray photoelectron spectroscopy (XPS). Test cells were assembled in an argon-filled glove box (MBRAUN), with Cu@SnS nanoelectrode as working electrode, Li foil as counter/reference electrode, polypropylene film (Celgard 2300) as separator, and 1 M LiPF$_6$ in a 1:1 (v/v) mixture of ethylene carbonate (EC) and diethyl carbonate (DEC) as electrolyte. Charge/ discharge cycles of the cells were measured using a Neware battery tester. Cyclic voltammograms (CVs) were measured at a scanning rate of 0.2 mV s^{-1}. Electrochemical impedance spectroscopy (EIS) measurements were performed in the frequency range of 10 mHz– 100 kHz with an AC voltage amplitude of 10 mV. CVs and EIS were performed using an IM6ex electrochemical analyzer.
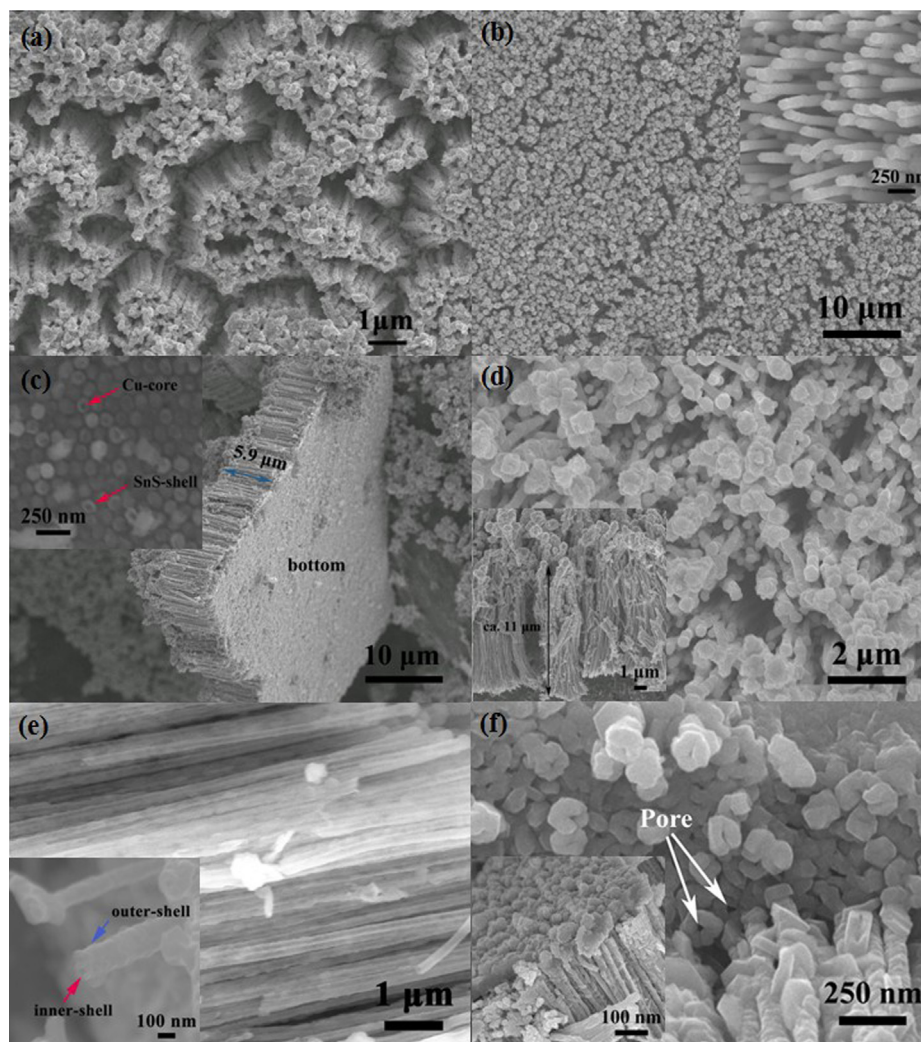
Fig. 2. FESEM images of samples fabricated under different experimental conditions: (a) top-view of Cu@SnS nanowire array obtained at room temperature; (b) nanowire agglomeration is mitigated by adopting Cu nanowires with larger diameter (inset); (c) cross-sectional view of the integrated Cu@SnS nanowire film manually scratched off the substrate, inset shows the bottom feature; (d) surface and cross-sectional (inset) images of the thicker nanowire array; (e) fractured cross-sections of the nanotubes obtained at 65 °C, (f) sample obtained with prolonged reaction time, inset shows the bottom image of the film spontaneously peeled off the substrate.

3. Results and discussion

The engineering concept of 3D-patterned Cu@SnS nano-electrode is schematically illustrated in Fig. 1a. With assistance of the uniform electric field distribution around each Cu nanowire along its entire length, nanoscale SnS can be conformally deposited on a large scale with uniformity. The expected equipotential curves and electrical force lines for a single nanowire are also depicted in Fig. 1a. Fig. 1b shows the top and bottom (inset) surfaces of the prepared AAM template. Theoretically, Cu nanowires grown in AAM template with small pore and large inter-pore spacing will be favorable for loading more active material after removing the template. Due to the surface tension force exerted on the nanowires during the evaporation of liquids, the arrays of high-aspect-ratio Cu nanowires with small diameters around 50 nm are inclined to agglomerate into thicker nanowire bundles, as indicated by Fig. 1c. We emphasize here that although the representative Cu@SnS nanowire forest with a thickness of ∼2 μm demonstrates the effectiveness of utilizing this 3D nanoarchitecture to promote SnS synthesis (see Fig. 1d), the existence of large void space between aggregated nanowire bundles indicates the space utilization needs to be further improved for increasing active material loading.

Fig. 2a shows the top-view FESEM images of the as-prepared Cu@SnS core–shell nanowire array with a deposition time of 10 min, it clearly reveals that every Cu nanowire is completely wrapped by a conformal SnS coating while the well alignment is inclined to deteriorate for nanowires with small diameters. Since the arrangement of the nanowires after template removal also strongly depends on the nanowire diameter or aspect ratio, the aligned Cu nanowires with larger diameter of ∼80 nm were intentionally used to verify whether size-optimization can alleviate the degree of nanowire agglomeration, as shown in the inset of Fig. 2b. As we can see from Fig. 2b, the surface roughness of SnS coating becomes pronounced as the deposition time is over 20 min, and meanwhile the gap between Cu nanowires is almost occupied by the deposited SnS. Fig. 2c shows the cross-sectional morphology of the Cu@SnS core–shell nanowire array manually scratched off the substrate with a thickness of ∼6 μm (the deposition time was 15 min), indicating the compactly stacked core–shell nanowires somehow ensure the structural integrity of electrode. Obviously, the solution-based reaction route for forming SnS is able to guarantee the coating the entire surface of Cu nanowire or filling the inter-nanowire spacing completely, even though the base array of Cu nanowires is very thick. As evidenced in the inset of Fig. 2c, for
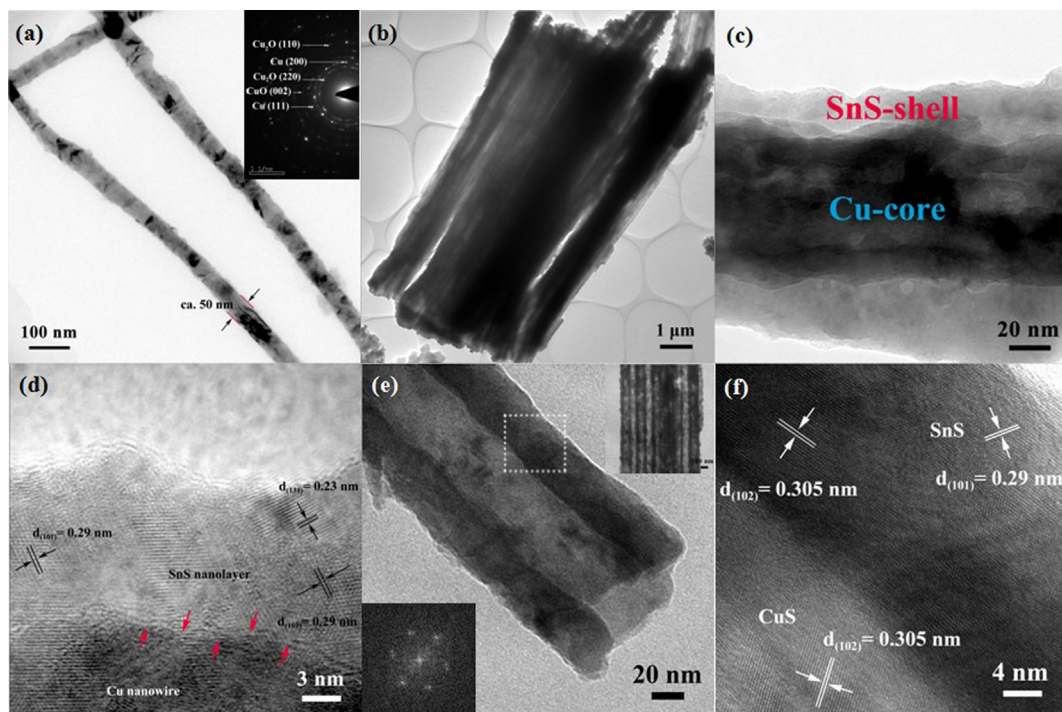
Fig. 3. (a) TEM image of the Cu nanowires with the corresponding SEAD pattern shown inset; (b) Cu@SnS nanowire bundles, (c) segmented individual Cu@SnS core−shell nanowire, and (d) shows the corresponding HRTEM image; (e) a segment of an individual SnS/CuS nanotube with open tips formed after completely dissolving Cu-core, inset shows the fast Fourier transform (FFT) pattern and TEM image of aligned nanotubes, (f) the corresponding HRTEM image of the nanotube.

every hybrid nanowire there is a Cu-core that directly connects it to the substrate, thus ensuring a reliable electrical connection for SnS sheath along the long axis of the Cu nanowire-core. As indicated by Fig. 2d, the hybrid Cu@SnS nanowires with embedded Cu nanowire cores of above 80 nm in diameter are more prone to retain alignment even they reached a length of 11 μm (inset of Fig. 2d). Meanwhile, an unexpected phenomenon was also observed in a specific condition, that is, tubular structure could be formed when the comparable kinetics of metal sulfides deposition and the Cu-core dissolution was achieved by simply elevating reaction temperature to 65 °C, as evidenced by the cross-sectional cracks of aligned nanotubes shown in Fig. 2e. Incomplete dissolution induced double-shell structure shown on the tip of an open nanotube (Fig. 2e inset) suggests that the core of Cu nanowire tends to be eroded faster than other parts, and the Kirkendall-type effect involving dominant outward mass transport during formation of the polycrystalline shells may partially explains the hollowing phenomenon [23]. Nonetheless, the newly formed tubular structure would get blocked again if further prolonging the reaction duration, as indicated in Fig. 2f. Moreover, the image shown in the inset of Fig. 2f indicates that the film-to-substrate adhesion was also adversely affected by the complete dissolution of Cu nanowire cores despite the nanofilm could be able to maintain structural integrity after peeling off the metallic substrate.
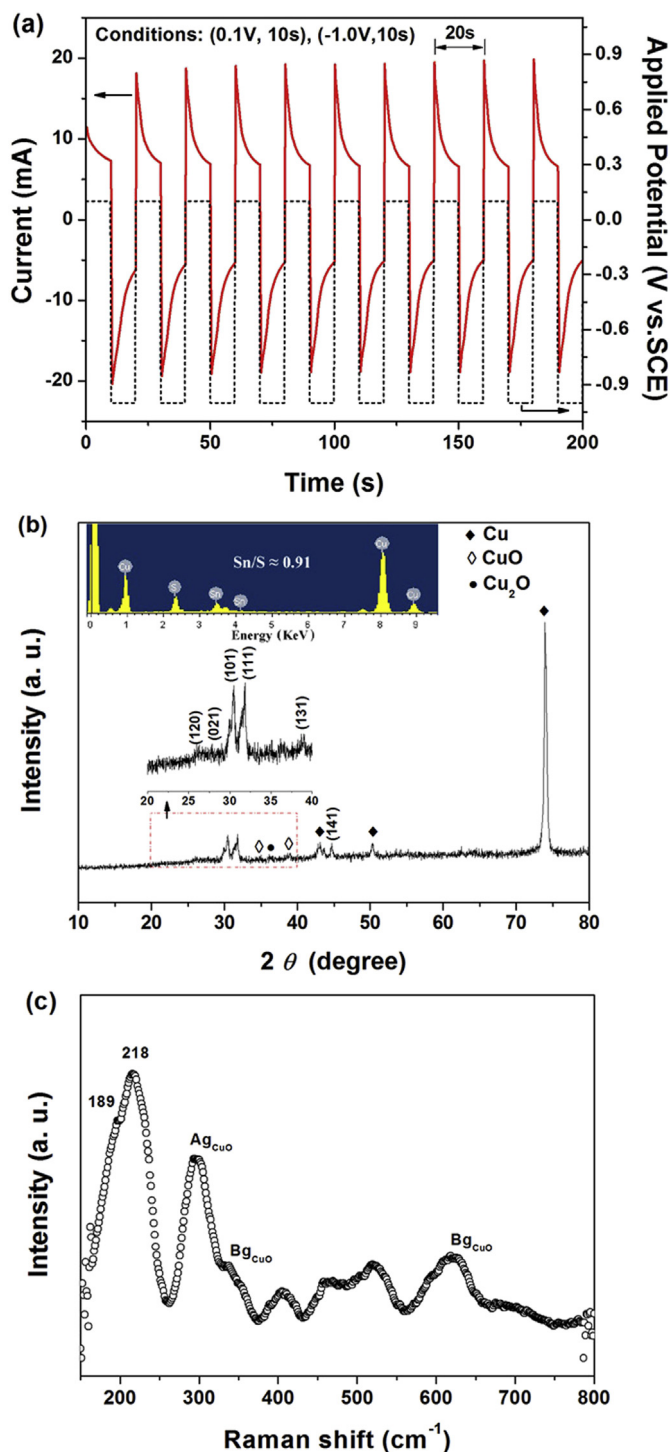
Fig. 3a shows the TEM image of bare Cu nanowires with 40−50 nm in diameter and several micrometers in length. Note that although the inset SEAD pattern in Fig. 3a indicates the existence of copper oxide impurities (CuO and Cu_2O) on the surface area of Cu nanowires, they could be irreversibly reduced to metallic copper during Li^+ intercalation at first discharge cycle [24]. The core−shell nanowire bundles shown in Fig. 3b indicate that most of the inter-nanowire space is occupied by the active material. Further evidence for the formation of the core−shell nanowire structure can be verified from the close TEM examination. As revealed in Fig. 3c, a compact SnS nanolayer (light area) with an average thickness of

∼20 nm formed along the axis of the Cu nanowire core (dark area) is distinguishable, and the lattice fringes of orthorhombic SnS with interplanar spacing, $d_{101} = 0.29$ nm and $d_{131} = 0.23$ nm, are clearly imaged in Fig. 3d where the crystallite sizes were found to vary from 3 to 15 nm, revealing its polycrystalline structure. It is worth mentioning that the prepared core−shell nanowires array can be assigned to Cu@SnS for simplicity, but more accurately expressed as $Cu/Cu_xO@SnS$ before undergoing the reduction process, considering the unavoidable surface oxidation of Cu nanowires occurred in ambient air or synthetic procedure. Meanwhile, TEM image in Fig. 3e further confirms that Cu nanowire cores could be dissolved in a relatively high-temperature acidic media, the hollow structures are clearly seen from a group of nanotubes with closely packed alignment (upper inset), and the fast Fourier transform (FFT) pattern (lower inset) indicates the formed nanotube is of polycrystalline phase. Accordingly, HRTEM image (Fig. 3f) taken from the dashed rectangle in Fig. 3e displays that the wall consists of nanocrystals with the lattice spacing of 0.305 nm and 0.29 nm, corresponding to the (102) and (101) planes of hexagonal CuS and orthorhombic SnS, respectively.

The possible formation mechanisms of the metal sulfide nanoelectrodes are now discussed. At room temperature, the chemically unstable $Na_2S_2O_3$ is very easy to separate out S in the acid solution, and the released nanoscale S adheres to the surface of Cu nanowire cathode could be further reduced to S^{2-} by applying a negative potential. Synchronously, the uniform formation of SnS nanolayers on Cu nanowires occurs when the ionic product of Sn^{2+} and S^{2-} exceeds the solubility product of SnS. The general reaction can be described by the following equation [15,16]:

$$2Sn^{2+} + S_2O_3^{2-} + 6H^+ + 8e^- \rightarrow 2SnS + 3H_2O \tag{1}$$
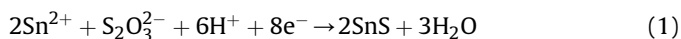
The selected pulsed potential and current profiles during deposition are shown in Fig. 4a. In principle, the potential-controlled negative pulse was applied to deposit SnS, and the
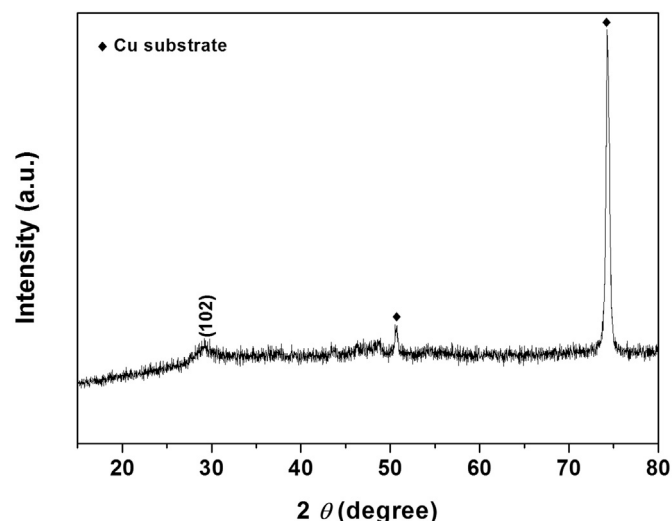
Fig. 4. (a) Pulsed-potential and the corresponding pulsed-current profiles during electrodeposition of SnS on Cu nanowires. (b) XRD pattern and EDS spectrum (inset) of the Cu@SnS nanoelectrodes. (c) Raman spectrum of the as-prepared Cu@SnS nanowires.

the HRTEM results shown in Fig. 3d. Besides, the weak diffraction peaks that corresponds to copper oxide (CuO and Cu_2O) should be ascribed to the relatively low quantity of impurity in the samples. In addition, quantitative EDX analysis further reveals that the atomic ratio of Sn to S of the resulting sample is close to the 1:1 stoichiometry (inset of Fig. 4b). The Raman spectrum shown in Fig. 4c was analyzed to ascertain the SnS phase and to look for the presence of traces of other components (SnS_2, Sn_2S_3) that are possible to deposit simultaneously. The band at around 218 cm^{-1} together with an overlapping band at 190 cm^{-1} belong to the A_g mode of SnS [25]. Besides, the Raman band observed at around 305 cm^{-1} can be assigned to the impurities of Sn_2S_3 and copper oxides [26]. It is assumed that the presence of small quantities of Sn_2S_3 phases (i.e. SnS + SnS_2) is due to side reaction of SnS and S during electrodeposition, and this explains the slight deviations from ideal stoichiometric SnS. Furthermore, the broad bands appear at 350–700 cm^{-1} should be assigned to the copper oxides originated from oxidation of Cu nanowire core [27,28], in correspondence with XRD and TEM findings.

Fig. 5 shows the XRD pattern of the metal sulfide nanotube array obtained at elevated temperature, the broad peak at $2\theta = 29.3°$ can be indexed to (102) plane of the hexagonal CuS phase (JCPDS card no. 6-464), which is in accordance with the HRTEM observation (Fig. 3f). The unapparent diffraction peak for SnS indicates a relatively small quantity of the compound formed in the sample. Besides, EDX analysis (not shown here) indicates that the Sn/S atomic ratio of the resulting hollow-structured sample decreases to about 1:3.5, implying the S^{2-} reacts with Cu^{2+} is in priority to Sn^{2+} at high temperature condition. Moreover, the surface atomic composition of the product was also investigated by XPS analysis. The binding energy values obtained in the XPS analysis were calibrated by referencing the C 1s peak to 284.60 eV. As shown in Fig. 6a, the peaks located at 486.5 and 495.0 eV are ascribed to the Sn $3d_{5/2}$ and Sn $3d_{3/2}$ of Sn^{2+}, respectively, which are in agreement with the accepted binding energy value for Sn–S bond of SnS. On the other hand, the XPS spectrum in Fig. 6b also shows two strong peaks around 933.1 and 953 eV, which are characteristics for Cu $2P_{3/2}$ and Cu $2P_{1/2}$, respectively. Besides, two shake-up satellite peaks at 942 and 962 eV are clearly seen, which might be due to the open $3d^9$ shell of Cu^{2+} ions. Obviously, the resulting S 2p spectrum in Fig. 6c shows one strong peak at a binding energy of 161.9 eV, which also agrees with the reference value for S^{2-} in SnS or CuS. Moreover, it is

following positive pulse was adopted to partially dissolve the already deposited SnS, especially the weakly bonded ones, which will make the deposits smooth and dense. The crystallographic structure of the Cu@SnS nanoelectrode is verified by XRD (Fig. 4b), the characteristic diffraction peaks at $2\theta = 30.5°$, 31.5° and 38.9° are attributed to (101), (111) and (131) planes of orthorhombic SnS (JCPDS card no. 39-0354) respectively, which are consistent with

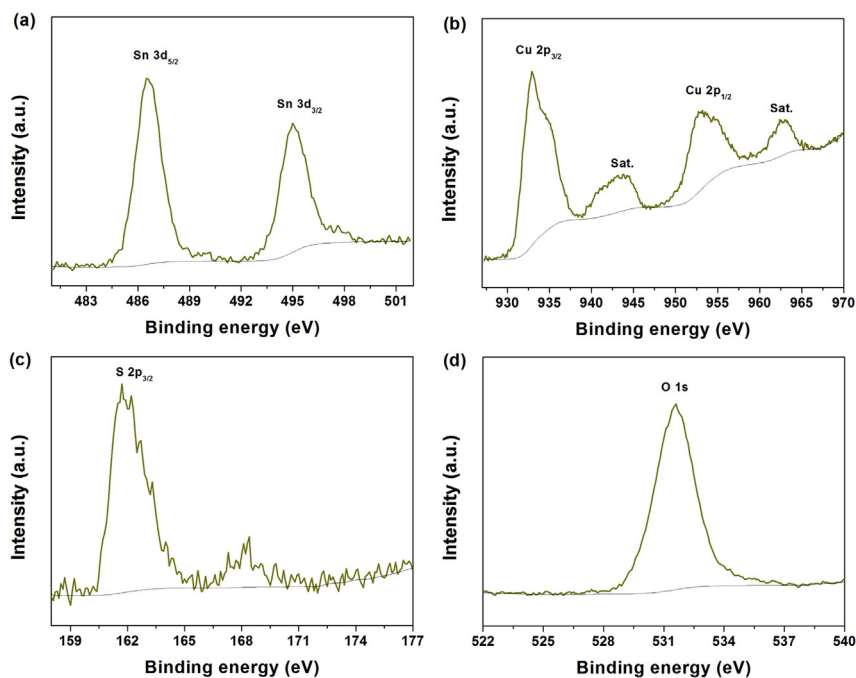**Fig. 5.** XRD pattern of the metal sulfide nanotube array.

Fig. 6. XPS spectra of the metal sulfide nanotube array: (a) Sn 3d, (b) Cu 2p, (c) S 2p and (d) O 1s.

clear that the position of the primary O 1s feature (ca. 531.4 eV) is assigned to the surface chemisorbed oxygen, whereas the shoulder at 529.8 eV for the lattice oxygen associated with metal oxides is hardly distinguished in Fig. 6d, further demonstrating the formation of CuS rather than CuO [23,29]. Based on above analyses, we infer that the formation of CuS phase and hollow structure originate from two processes: (i) At elevated temperature, anomalous

dissolution of Cu nanowire cores under cathodic polarization in oxygen-containing acidic media leads to the formation of hollow structure combining the release of Cu^{2+} ions [30,31]; (ii) The reaction of S^{2-} ions with newly released Cu^{2+} ions to form CuS: $Cu^{2+} + S^{2-} \rightarrow CuS$, and this means Cu nanowires with small diameter could not only serve as conducting matrix for boosting the electrochemical synthesis, but also as a sacrificial template for
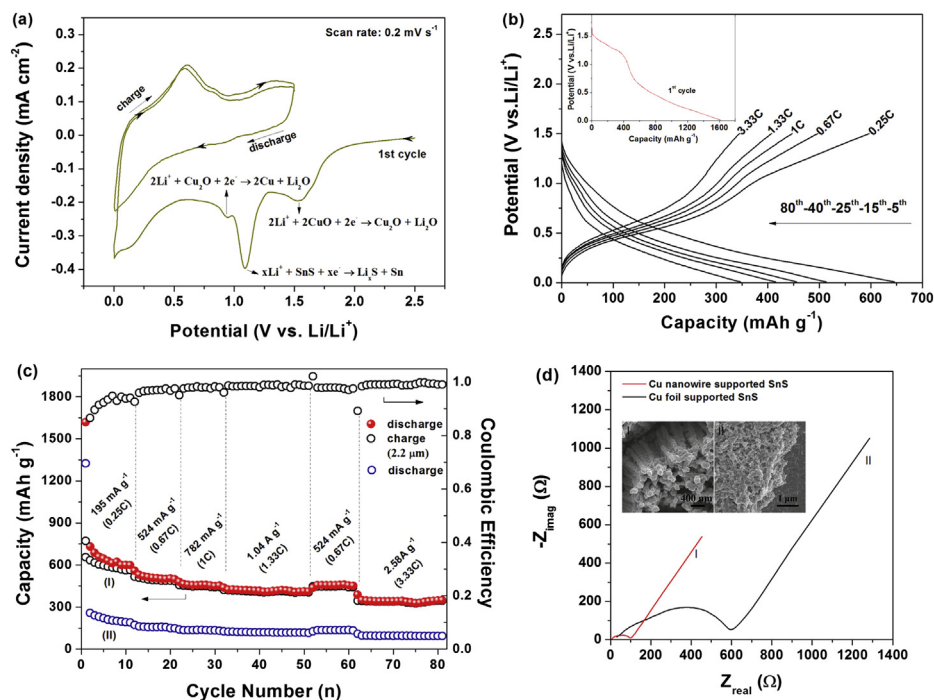

Fig. 7. Electrochemical properties of Cu@SnS nanoelectrodes: (a) CV plots; (b) representative galvanostatic charge/discharge curves at specific rates; (c) cycling performance of the electrodes obtained at different rates; (d) Nyquist plots of SnS formed on nanostructured and planar current collectors (measured at 0.5 V) with corresponding electrode images are shown as insets.
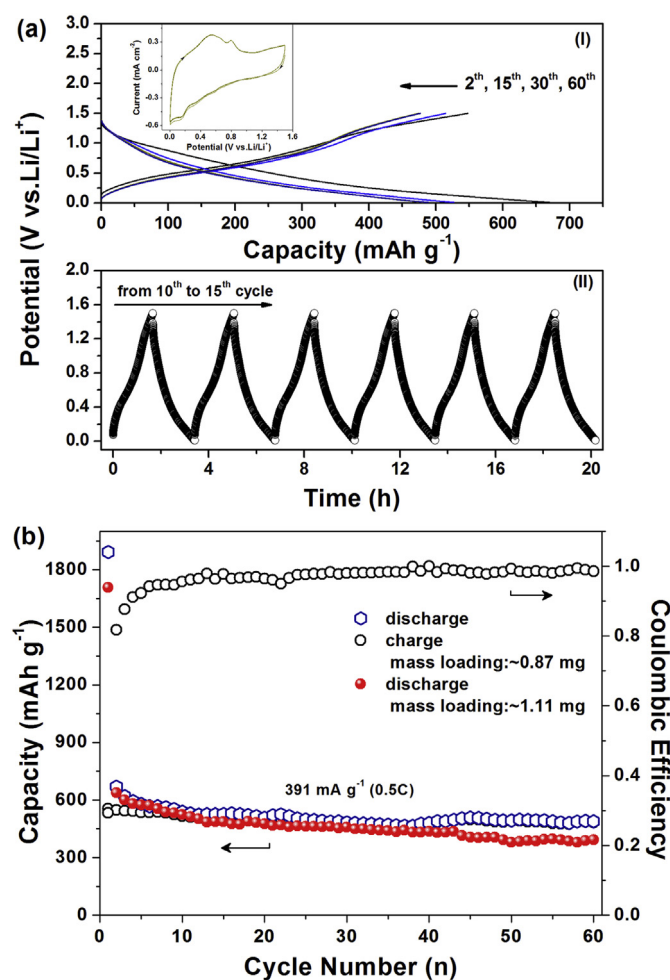
Fig. 8. (a) The representative galvanostatic charge/discharge curves with the CV curve inset (I), and the corresponding potential vs. time profile (II); (b) cycling stability of thicker Cu@SnS nanowire array with different mass loading.

building tubular structure materials. However, deeper insight towards revelation of exact formation mechanism for CuS/SnS nanotube array is the subject of further ongoing research.

We next investigate the applicability of the resulting nanoelectrodes towards electrochemical energy storage. Regarding the novel CuS/SnS nanotube array, despite the drawback concerning

poor film-to-substrate adhesion caused by the complete removal of Cu-core adversely affects the application of CuS/SnS nanotube array, we can still anticipate that the well-organized tubular structure (facilitates easy penetration of electrolyte) and possible synergetic effects between two components could be helpful to improve the electrochemical performance of the metal sulfate nanoelectrode when charged/discharged within a specific operating voltage window; Moreover, further incorporating other functional materials or inorganic solid electrolyte into the nanochannels of the CuS/SnS nanotube array can promisingly make it a competitive cathode material [32–35]. Alternatively, we just focus on evaluating the Li$^+$ storage capability of Cu@SnS nanoelectrodes at this stage. The CV measurement shown in Fig. 7a reveals the Li$^+$ extraction/insertion mechanisms and kinetics occurring on cycling the Cu@SnS nanoelectrode. The cathodic peaks appear at around 1.5 and 1.1 V during first cycle could be attributed to the decomposition of the surface copper oxide impurities and SnS (xLi$^+$ + SnS + xe$^-$ → Li$_x$S + Sn), accompanied with the formation of solid electrolyte interface (SEI), which are responsible for the large irreversible capacity loss between the first and second cycles [11,23,36]. Besides, the cathodic peak emerges from 0.5 to 0 V can be ascribed to the reversible intercalation of Li$^+$ into Sn, xLi$^+$ + Sn + xe$^-$ → Li$_x$Sn, while the corresponding anodic peak is located at ~0.6 V. It should be emphasized that the produced Li$_x$S phase, analogy to the role of Li$_x$O phase in SnO$_2$ or SnO [37], could also act as an inactive component for buffering volume expansion during cycling process [38].

To confirm whether the enhancement in kinetics and structural stability can improve the charging/discharging behavior of electrochemically synthesized SnS, we evaluated the Li$^+$ storage performance of the Cu@SnS nanoelectrode in rate-varying model. Fig. 7b shows the representative charge/discharge curves of the nanoelectrode (film thickness: 2.2 μm), which intuitively exhibit that the corresponding specific capacities are varied along with the current rates, changing from 645.7 (0.25C) to 347.2 mAh g^{-1} (3.33C) (note that here C does not have the usual meaning but is defined as 782 mA g^{-1} in this study for easy donation). In particular, as indicated in Fig. 7c, the cycling response at continuously varying rates shows that even when cycled at a relatively high rate of 1.33C, comparable capacities of ~410 mAh g^{-1} can still be retained. Moreover, a discharge capacity of about 451.2 mAh g^{-1} with a coulombic efficiency of 98% is obtained when the current density is again reduced back to 524 mA g^{-1} (0.67C) after more than 30 cycles, showing a good retention property. Upon subsequent cycles, the rate is increased to a higher value of 3.33C (charge/discharge time: ~18 min), the electrode can still deliver a stable capacity of
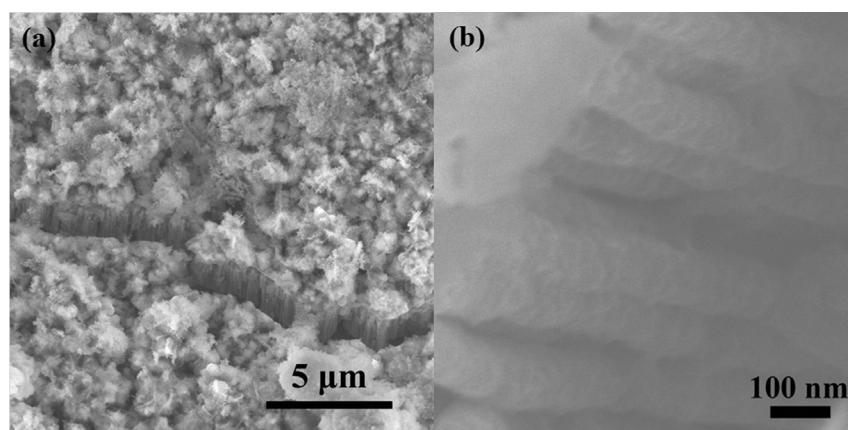
Fig. 9. (a) Surface morphology of the Cu@SnS nanoelectrode underwent 80 charge/discharge cycles and (b) its magnified cross-sectional image.

about 348 mAh g^{-1} after another 20 cycles. Remarkably, such rate capability far surpasses those of previously reported SnS nanoparticles even with carbon-coatings [10].

As demonstrated by the cycling performance of the SnS layer directly deposited on planar Cu foil (curve (II) in Fig. 7c), it gives only a reversible capacity of 131 mAh g^{-1} (1C), in contrast to a significantly higher capacity of 451 mAh g^{-1} (1C) achieved with 3D-patterned Cu@SnS nanoelectrode. On an areal capacity basis, the Cu@SnS nanoelectrode (about 2 μm film thickness with a mass loading of ~0.43 mg cm^{-2}) and its planar counterpart (~0.71 mg cm^{-2}) delivered an areal capacity of ~194 and 93 μAh cm^{-2}, respectively, after 15 cycles. Again, this result clearly indicates simply increasing the film thickness by prolonging deposition time will not only reduce the quality of the deposited SnS layer but also increase the current path length, thus leading to drastic capacity loss or poor utilization of the active material for the planar electrode.

Remarkably, the coulombic efficiency of the nanoelectrode in 3D-patterned configuration rapidly increases from 75% in the 1st cycle to 99.5% in the 5th cycle and it maintains above 99% regardless of the rate changing (Fig. 7c), showing a good reversibility. The phenomenon of the capacity decreases as the current density increasing could be interpreted by the depth-dependent lithiation through the electrode, namely, full storage capacity could not been reached at high current rates because of kinetic limitations associated with the diffusion of Li^{+} through the active materials. However, the increase of charge/discharge rate promotes the reversibility of the Li^{+} intercalation reaction at the interface between the solid electrode and the liquid electrolyte, and this explains the greater coulombic efficiency observed at high current rates. Additional insight into the electrochemical kinetics of lithiation behaviors for the prepared nanoelectrode is obtained by EIS investigation. As depicted in Fig. 7d, the dramatically depressed semicircle of SnS formed on aligned Cu nanowires clearly indicates a higher charge-transfer rate of Li^{+} in the electrode as compared to that of the loose SnS layer formed on planar substrate. As a result, the improved electrical conductivity of the Cu@SnS nanoelectrode could facilitate charge transport accompanying rapid intercalation reactions at the interface, thus allowing remarkable capacity retention under high current rates.

Little question remains that this electrode configuration can boost capacity scaling by simply adjusting the film thickness. Curve I in Fig. 8a shows the selected charge/discharge curves of the thicker Cu@SnS nanoelectrode, and the corresponding CV curve (inset) exhibited higher current densities compared with the thin films at the same scan rate. Besides, as indicated in curve II of Fig. 8a, it only took ~3.5 h to complete a charge/discharge cycle for Cu@SnS nanoelectrode at 0.5C rate, corresponding to a factual C-rate of ~0.75C, and this discrepancy can be ascribed to the impurities induced actual capacity of electrode material is lower than 782 mAh g^{-1}. Moreover, particularly noteworthy are the results depicted in Fig. 8b, excellent cyclability of the electrode is almost unaffected by increasing the film thickness to ~6 μm, namely producing a reversible capacity of ~489 mAh g^{-1} at 0.5C with a coulombic efficiency of 98.5% after 60 cycles (areal capacity is ~425 μAh cm^{-2}), thus suggesting the effectiveness of 3D-patterned nanoarchitecture in utilizing the out-of-plane dimension to scale the charge-storage capacity. Indeed, this feature can make the Cu@SnS nanoelectrode more competitive than self-supported SnS films for Li-ion microbattery application, since simply making the latter films thicker for storing more energy will probably result in dramatic reduction in power density arising from electrical failures. However, the accelerated capacity fading occurred as the deposition time was further prolonged to 40 min, as shown in Fig. 8b, which suggests the excessive SnS covering the top of the Cu

nanowires failed to take advantage of the merits of the specific nanostructure efficiently.

As shown in Fig. 9, the electrode maintains good structural integrity except the surface is covered with electrolyte salts, and the SnS-shell is still tightly attached to the Cu nanowire-core without apparent structural alteration after 80 cycles, confirming the robustness of the 3D-patterned nanostructure with enhanced resistance to crack initiation and propagation. Hence, in addition to the improved quality of SnS deposits itself and small inter-nanowire spacing available for easy electrolyte penetration, the remarkable electrochemical performance is believed to originate from the ideal core–shell nanoarchitecture, in which Cu nanowire-core functions not only as built-in "nanoelectronic wire" for enabling fast electron transport but also as a stable matrix for supporting SnS sheath layer upon lithium uptake or release.

4. Conclusions

In summary, we have identified the effectiveness of core–shell nanoarchitecture to endow the electrochemically synthesised SnS with superior Li^{+} storage capability. With the prominent feature that allows for achieving high power and energy densities on a small footprint area, the prepared Cu@SnS nanoelectrodes should have promising prospect for the Li-ion microbattery application. Moreover, besides providing a potential building blocks for nanoscale devices, the innovative electrochemical fabrication of CuS/SnS nanotube array may boost the application research of metal sulfide nanoelectrodes in the fields of energy storage and conversion.

References

[1] T.S. Arthur, D.J. Daniel, N. Cirigliano, D.C. Johnson, P. Malati, J.M. Mosby, E. Perre, M.T. Rawls, A.L. Prieto, B. Dunn, MRS Bull. 36 (2011) 523–531.
[2] J.F.M. Oudenhoven, L. Baggetto, P.H.L. Notten, Adv. Energy Mater. 1 (2011) 10–33.
[3] M. Nathan, D. Golodnitsky, V. Yufit, E. Strauss, T. Ripenbein, I. Shechtman, S. Menkin, E. Peled, J. Microelectromech. Syst. 14 (2005) 879–884.
[4] P.G. Bruce, B. Scrosati, J.M. Tarascon, Angew. Chem. Int. Ed. 47 (2008) 2930–2946.
[5] Y.G. Guo, Y.S. Hu, W. Sigle, J. Maier, Adv. Mater. 19 (2007) 2087–2091.
[6] Z. Deng, D. Cao, J. He, S. Lin, S.M. Lindsay, Y. Liu, ACS Nano 6 (2012) 6197–6207.
[7] K. Aso, A. Hayashi, M. Tatsumisago, Cryst. Growth Des. 11 (2011) 3900–3904.
[8] K. Chang, Z. Wang, G.C. Huang, H. Li, W.X. Chen, J.Y. Lee, J. Power Sources 201 (2012) 259–266.
[9] Q. Wu, L.F. Jiao, J. Du, J.Q. Yang, L.J. Guo, Y.C. Liu, Y.J. Wang, H.T. Yuan, J. Power Sources 239 (2013) 89–93.
[10] Y. Li, J.P. Tu, X.H. Huang, H.M. Wu, Y.F. Yuan, Electrochim. Acta 52 (2006) 1383–1389.
[11] Y. Li, J.P. Tu, X.H. Huang, H.M. Wu, Y.F. Yuan, Electrochem. Commun. 9 (2007) 49–53.
[12] J.G. Kang, J.G. Park, D.W. Kim, Electrochem. Commun. 12 (2010) 307–310.
[13] D.D. Vaughn II, O.D. Hentz, S. Chen, D. Wang, R.E. Schaak, Chem. Commun. 48 (2012) 5608–5610.
[14] J.J. Cai, Z.S. Li, P.K. Shen, ACS Appl. Mater. Interfaces 4 (2012) 4093–4098.
[15] A. Ghazali, Z. Zainal, M.Z. Hussein, A. Kassim, Sol. Energy Mater. Sol. C 55 (1998) 237–249.
[16] N. Sato, M. Ichimura, E. Arai, Y. Yamazaki, Sol. Energy Mater. Sol. C 85 (2005) 153–165.
[17] J.R.S. Brownson, C. Georges, C. Lévy-Clément, Chem. Mater. 18 (2006) 6397–6402.
[18] A. Zaban, A. Meier, B.A. Gregg, J. Phys. Chem. B 101 (1997) 7985–7990.
[19] P.L. Taberna, S. Mitra, P. Poizot, P. Simon, J.M. Tarascon, Nature 5 (2006) 567–573.
[20] J. Hassoun, S. Panero, P. Simon, P.L. Taberna, B. Scrosati, Adv. Mater. 19 (2007) 1632–1635.

[21] L. Bazin, S. Mitra, P.L. Taberna, P. Poizot, M. Gressier, M.J. Menu, A. Barnabé, P. Simon, J.-M. Tarascon, J. Power Sources 188 (2009) 578–582.
[22] C.Y. Han, G.A. Willing, Z.L. Xiao, H.H. Wang, Langmuir 23 (2007) 1564–1568.
[23] C.Y. Wu, S.H. Yu, S.F. Chen, G.N. Liu, B.H. Liu, J. Mater. Chem. 16 (2006) 3326–3331.
[24] Z.G. Yin, Y.H. Ding, Q.D. Zheng, L.H. Guan, Electrochem. Commun. 20 (2012) 40–43.
[25] S.Y. Cheng, Y.J. He, G.N. Chen, E. Cho, G. Conibeer, Surf. Coat. Technol. 202 (2008) 6070–6074.
[26] S.B. Wang, C.H. Hsiao, S.J. Chang, K.T. Lam, K.H. Wen, S.C. Hung, S.J. Young, B.R. Huang, Sens. Actuators A Phys. 171 (2011) 207–211.
[27] Y.C. Mao, J.T. He, X.F. Sun, W. Li, X.H. Lu, J.Y. Gan, Z.Q. Liu, L. Gong, J. Chen, P. Liu, Y.X. Tong, Electrochim. Acta 62 (2012) 1–7.
[28] S.H. Wang, Q.J. Huang, X.G. Wen, X.Y. Li, S.H. Yang, Phys. Chem. Chem. Phys. 4 (2002) 3425–3429.
[29] X. Zhang, Y.G. Guo, P.Y. Zhang, Z.S. Wu, Z.J. Zhang, Mater. Lett. 64 (2010) 1200–1230.
[30] A.J. Read, J. Phys. Chem. 76 (1972) 3656–3663.
[31] V. Kreizer, I.K. Marchakov, N.M. Tutukina, I.D. Zartsyn, Prot. Met. 39 (2003) 35–39.
[32] J.S. Chung, H.J. Sohn, J. Power Sources 108 (2002) 226–231.
[33] Y.H. Chen, C. Davoisne, J.M. Tarascon, C. Guéry, J. Mater. Chem. 22 (2012) 5295–5299.
[34] H. Mazor, D. Golodnitsky, L. Burstein, E. Peleda, Electrochem. Solid-State Lett. 12 (2009) A232–A235.
[35] Y.R. Wang, X.W. Zhang, P. Chen, H.T. Liao, S.Q. Cheng, Electrochim. Acta 80 (2012) 264–268.
[36] A. Débart, L. Dupont, P. Poizot, J.B. Leriche, J.M. Tarascon, J. Electrochem. Soc. 148 (2001) A1266–A1274.
[37] B. Liu, Z.P. Guo, G.D. Du, Y.N. Nuli, M.F. Hassan, D.Z. Jia, J. Power Sources 195 (2010) 5382–5386.
[38] G.C. Huang, T. Chen, Z. Wang, K. Chang, W.X. Chen, J. Power Sources 235 (2013) 122–128.